

Load–deflection of flexible ring-net barrier in resisting debris flows

YONG KONG*, XINGYUE LI†, JIDONG ZHAO‡ and MINGFU GUAN§

Quantitative understanding of the load–deflection mechanisms of a flexible barrier in intercepting debris flows is critical for barrier design, but remains practically challenging due to the difficulties involved in capturing multi-phase, multi-way interactions. This study employs a physics-based coupled computational fluid dynamics and discrete-element method (CFD–DEM) to simulate a flexible ring-net barrier as a permeable, deformable multi-component system by DEM and model a debris flow as a mixture of discrete particles and a continuous slurry by DEM and CFD, respectively. The CFD–DEM coupling framework offers a unified treatment of in-flow solid–fluid interaction, flow–barrier interaction and interactions among barrier components. Numerical predictions of key flow–barrier interactions and cable forces show reasonable consistency with large-scale experiments. Systematic simulations with varying flow–barrier height ratios ε and flow dynamics are performed to examine the evolving mechanisms of load sharing and transmission and quantify the ε -dependent load–deflection modes. The ratio ε is found to bear a strong, positive correlation with the key barrier response in three typical modes. The post-peak barrier deformations experience shrinkages with $\varepsilon \leq 0.6$ and expansions when $\varepsilon > 0.6$. This study helps to improve understanding of the load–deflection mechanisms for practical design of flexible barriers in mitigating debris flows.

KEYWORDS: debris flow; disaster risk reduction; flexible ring net barrier; geohazard mitigation; load–deflection mechanism; numerical modelling

INTRODUCTION

Flexible barriers have been increasingly adopted worldwide to mitigate debris flows, debris/rock/snow avalanches and rockfalls, in the wake of increased frequency and magnitude of cascading geophysical flows due to climate-driven rainstorms, severe wildfires and a changing landscape (Pisano *et al.*, 2017; Hoch *et al.*, 2021; Li *et al.*, 2022). Compared with rigid barriers (Ng *et al.*, 2018; Marchelli *et al.*, 2020), flexible barriers arrest geophysical flows by virtue of their high permeability and structural deformability to mobilise complicated load–deflection behaviour, thereby prolonging impact duration and attenuating the peak impact (Ashwood & Hungr, 2016; Song *et al.*, 2019). Understanding the load–deflection mechanisms is critical when evaluating the peak impact, barrier deformation and retainment capacity for practical designs (Kwan & Cheung, 2012; EOTA, 2016). However, challenges remain in realistically capturing and quantifying the intricate multi-way interactions between a deformable, permeable barrier system and both the solid and fluid in impinging the flows. The impact process features various mechanisms governing force sharing, transmission and redistribution, energy dissipation and transformation, phase separation and flow regime transition, posing great difficulties for modelling and analysis.

Existing studies on debris flows interacting with flexible barriers can be largely described by two methodological categories: experimental and numerical approaches. Both full-scale and large-scale experimental tests have been carried out to examine the impact process (Bugnion *et al.*, 2012; Brighenti *et al.*, 2013; Vicari *et al.*, 2022). These studies provide valuable data and help to offer a better understanding of the subject. However, they are mostly limited by various constraints and can be costly. Capturing the overflow processes and examination of crucial force sharing and transferring among barrier components remain practically difficult (DeNatale *et al.*, 1999; Ferrero *et al.*, 2015). Small-scale experiments have been used as an alternative to investigate key controlling factors of the flow–barrier interactions under well-controlled conditions (Ashwood & Hungr, 2016; Ng *et al.*, 2017). Nonetheless, they commonly resort to the use of idealised or simplified flexible barriers such as impermeable membranes (Ashwood & Hungr, 2016; Song *et al.*, 2021) and uniform plastic meshes (Wendeler *et al.*, 2019), which may fail to recover the inherent permeability, non-uniformity and mechanical characteristics of flexible barriers.

Numerical approaches have been widely developed to analyse flow-resisting flexible barriers. Notable studies include continuum-based methods (the material point method (MPM) (Ng *et al.*, 2020); finite-element method (FEM) (Zhao *et al.*, 2020); smoothed particle hydrodynamics (SPH) (Fávero Neto *et al.*, 2020; Bui & Nguyen, 2021); discrete-based methods, e.g. the discrete-element method (DEM) (Zhu *et al.*, 2019); and coupled approaches, e.g. the lattice Boltzmann method (LBM) coupled with DEM and FEM (Leonardi *et al.*, 2016), coupled FEM–DEM (Liu *et al.*, 2020), coupled computational fluid dynamics and DEM (CFD–DEM) (Kong *et al.*, 2021a)). In practice, a flexible ring-net barrier commonly comprises a ring net, cables and energy dissipators (Fig. 1(a)), which are rarely captured in a unified method. Importantly, these components can significantly interact with one another in addition to their interactions with impinging flows. The

Manuscript received 17 April 2022; revised manuscript accepted 8 November 2022. First published online ahead of print 21 November 2022.

Discussion on this paper closes on 1 September 2024, for further details see p. ii.

* Department of Civil Engineering, The University of Hong Kong, Hong Kong SAR, P. R. China (Orcid:0000-0002-1879-7682).

† Department of Geotechnical Engineering, College of Civil Engineering, Tongji University, Shanghai, P. R. China.

‡ Department of Civil and Environmental Engineering, The Hong Kong University of Science and Technology, Hong Kong SAR, P. R. China (Orcid:0000-0002-6344-638X).

§ Department of Civil Engineering, The University of Hong Kong, Hong Kong SAR, P. R. China (Orcid:0000-0002-5684-4697).

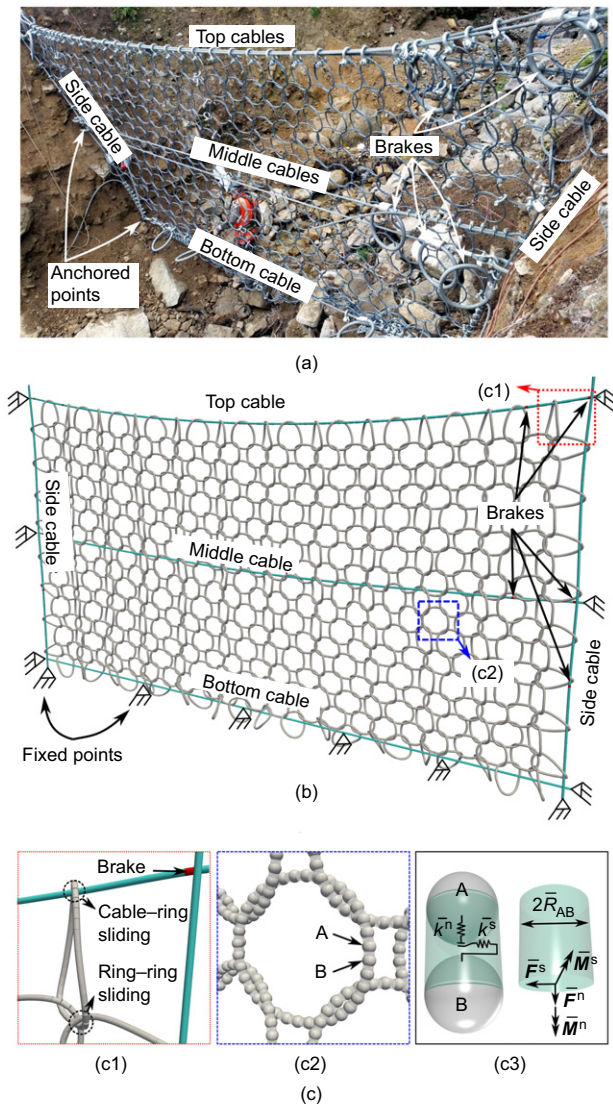


Fig. 1. Modelling of a flexible ring-net barrier system: comparison between (a) a full-scale flexible ring-net barrier in New Zealand (GEOVERT, 2016) and (b) a reduced-scale flexible ring-net barrier (by DEM); (c) part (c1) a zoom window showing the connections among ring elements, cables and brakes; part (c3) representing a parallel bond and its key parameters (Li *et al.*, 2020) adopted to describe the remote interaction between particles A and B shown in part (c2)

in-barrier interacting processes such as cable–ring–ring frictional sliding and curtain effect constitute crucial resisting mechanisms for the barrier (Coulibaly *et al.*, 2018), which are vital in the accurate prediction of barrier deformation, load sharing and transmission. However, current studies (Leonardi *et al.*, 2016; Liu *et al.*, 2020; Zhao *et al.*, 2020; Kong *et al.*, 2021a) commonly generate the net units in a two-dimensional (2D) plane by ignoring cable–ring–ring sliding in three-dimensional (3D) space. Furthermore, the solid–liquid nature of a debris flow plays a crucial role in predicting its propagation and impact (Iverson, 1997; Pudasaini & Mergili, 2019; Tayyebi *et al.*, 2021) but has commonly been simulated as continuum flows or dry flows (Albaba *et al.*, 2017; Zhu *et al.*, 2019; Ng *et al.*, 2020). There is a pressing need for a physics-based, unified numerical tool that can consider all these aspects, such as the multi-way interactions and cable–ring–ring frictional sliding.

Despite the complexity of the load–deflection process of a flexible barrier in resisting the impact of debris flow, the

current practice of barrier design has been built upon using an oversimplified spring model, assuming a constant barrier equivalent stiffness k_b^n , to calculate the normal impact load F_b by $F_b = k_b^n D_h$, where D_h denotes the maximum barrier deflection parallel to the flow direction. The model has been examined against data from small-scale and full-scale tests (e.g. Ashwood & Hungr, 2016; Wendeler, 2016; Song *et al.*, 2019). Based on back-calculation of field events, Wendeler (2016) reported a relationship between k_b^n and D_h by the neglect of the occurrence of possible energy losses and outlet materials. Notably, Song *et al.* (2019) reported a two-stage development trend of barrier stiffness based on small-scale centrifuge tests equipped with a novel flexible barrier composed of membrane and cables. They calculated F_b by the simplified solution based on cable forces and deformed angles (Ng *et al.*, 2017). Nevertheless, the estimation of F_b is challenging, as it is not directly measurable in experiments or in the field. Thus, the combined effects of over-simplified flexible barriers, idealised assumptions and difficult-to-estimate variables (e.g. forces and deformations) pose severe difficulties when clarifying the interplay among barrier loads, deflections and deformation features such as the barrier equivalent stiffness.

Moreover, flow features (e.g. dynamics, components and the flow–barrier height ratio ε) are critical for understanding the load–deflection mechanism and thus essential for analysing and designing a flexible barrier. Note that the ratio is defined as $\varepsilon = h_0/h_b$, where h_0 and h_b are the pre-impact flow height and the height of an undeformed barrier, respectively. Current studies mainly focus on the effects of flow dynamics and components on the impact behaviours (Ashwood & Hungr, 2016; Wendeler, 2016; Song *et al.*, 2019). Existing analytical models for the design of flexible barriers (e.g. Ferrero *et al.*, 2015; Song *et al.*, 2021) also do not explicitly consider the ratio ε . Nonetheless, several studies indicate that the ratio ε could largely affect the impact behaviours and mechanisms (Hákonardóttir *et al.*, 2003; Faug, 2015; Ng *et al.*, 2018). The influence of the ratio ε on the load–deflection responses of flexible barriers in mitigating debris flows remains an open question. To address this issue, a systematic numerical investigation based on a coupled CFD–DEM approach is conducted in this study.

METHODOLOGY AND MODEL SET-UP

A unified, unresolved CFD–DEM coupling method is employed to obtain 3D solutions to such multi-phase, multi-physics flow–structure interaction problems. The debris flow is treated as a mixture of solid particles and viscous liquid (Fig. 2(b)); these are simulated by DEM and CFD, respectively. A flexible barrier is modelled by DEM (Fig. 1(b)). The translational and rotational motions of each particle in the DEM are governed by Newton’s equations, and the fluid in CFD is controlled by the locally averaged Navier–Stokes equation for each fluid cell. The two-way coupling scheme offers a unified way for the convenient description of solid–liquid interactions in a debris flow and between barrier components and the debris liquid. Free surfaces are simulated by the volume-of-fluid (VOF) method implemented in CFD. The employed method has been benchmarked with classic geomechanics problems (Zhao & Shan, 2013; Li & Zhao, 2018) and has been shown to capture the complicated fluid–solid interactions in various engineering conditions, including the flow–barrier interactions (Li *et al.*, 2021; Kong *et al.*, 2021b). This method has been further extended to examine debris-flow impacts on flexible barriers (Li *et al.*, 2020; Kong *et al.*, 2021a), where the modelling of different barrier components has been further enriched, calibrated and verified. Details of the governing equations solved by the

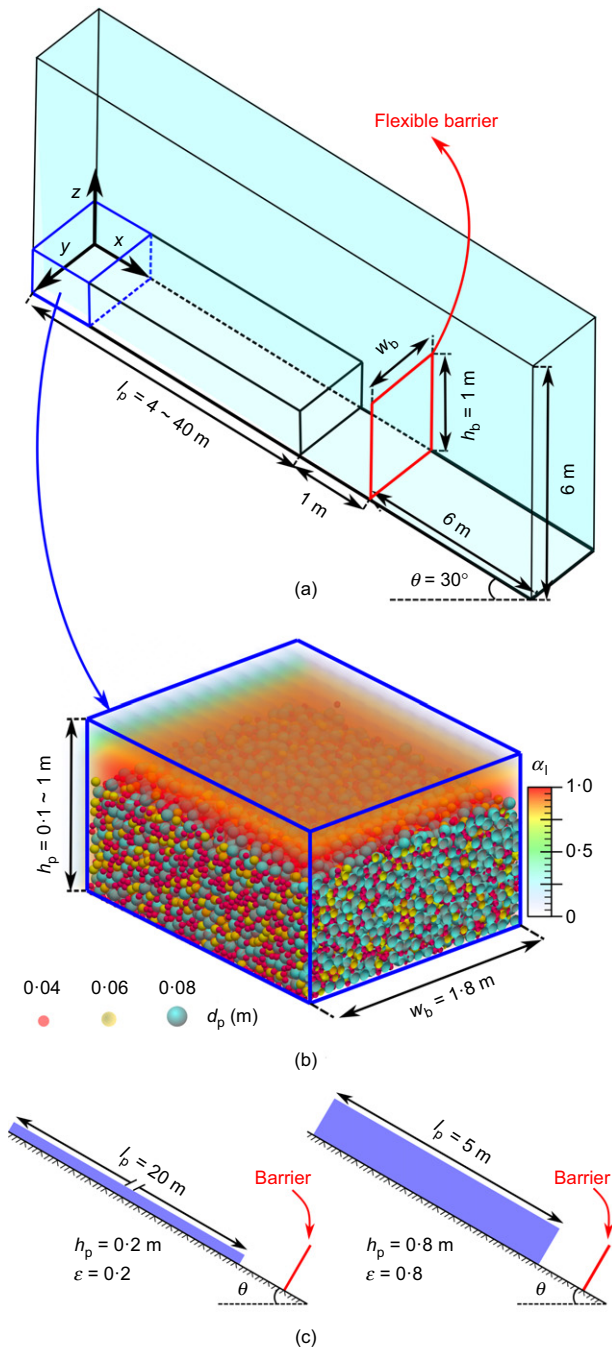


Fig. 2. Model set-up: (a) model geometry prior to the release of the mixture; (b) illustration of a representative part of a mixture sample; (c) illustration of two representative cases with the flow-barrier height ratios ϵ equal to 0.2 (left) and 0.8 (right). α_l denotes liquid volume fraction

coupled CFD-DEM method have been described in Kong *et al.* (2021a) and Zhao & Shan (2013), and will not be repeated here for the sake of brevity.

Modelling of a flexible ring-net barrier system

The study considers a typical trapezoidal-shaped flexible barrier system composed of a ring net, brake elements and cables, as shown in Fig. 1(a), that is used in New Zealand (GEOVERT, 2016) for mitigating debris flows. It is typically fixed on three sides (left, bottom and right) by anchors and nails driven into the ground. The DEM is used to model such a flexible barrier by assembling a ring net consisting of 382

interlocking rings, five supporting cables and ten brake elements (Fig. 1(b)). The cables are designed to sustain the load transferred from the ring net and further to anchored boundaries (Figs 1(a) and 1(b)). The bottom cable and lateral edges of both the top and middle cables (Fig. 1(b)) are fixed to mimic the anchored boundaries (Fig. 1(a)). Both ends of a horizontal supporting cable are equipped with two brake elements (Figs 1(a) and 1(b)) designed to dissipate impact energy and lengthen significantly under debris-flow impact. Consequently, the lengthened cable can better carry the orthogonal loads than a straight spanned one. Fig. 1(c), part (c1) presents the intricate connections among interlocking rings, cables and brake elements where the cable-ring-frictional sliding and collision are enabled.

All the barrier components are modelled by DEM using nodal particles connected with parallel bonds (Potyondy & Cundall, 2004; Kong *et al.*, 2021a). Fig. 1(c), part (c1) demonstrates that the interlocking ring elements are idealised into numerical meshes with a set of nodal particles placed at the physical nodes of the ring (Fig. 1(c), part (c2)). Fig. 1(c), part (c3) represents the parallel bond linking the nodal particles A and B in a ring element (Fig. 1(c), part (c2)). This bond can sustain the axial and shear-directed forces and moments, which are denoted by \vec{F}^n , \vec{F}^s and \vec{M}^n , \vec{M}^s , respectively. Specifically, five parameters are used to define a parallel bond: the normal and shear stiffnesses per unit area, \vec{k}^n and \vec{k}^s ; the tensile and shear strengths, $\vec{\sigma}_c$ and $\vec{\tau}_c$; and the bond-radius multiplier $\vec{\lambda}$. The radius of a parallel bond \vec{R}_{AB} is defined as $\vec{R}_{AB} = \vec{\lambda}_{\min}(R_A, R_B)$, where R_A and R_B are radii of two connected particles A and B. Interested readers may refer to the literature (Potyondy & Cundall, 2004; Li *et al.*, 2020) for further detail.

Similarly, a cable is modelled with a set of connected nodal particles whose centres are along the cable, and a brake element is modelled with two connected nodal particles. Different types of parallel bonds can be handily adopted to capture various behaviours of the barrier components. Note that brake elements exhibiting highly non-linear behaviour are modelled by a piecewise linear plasticity model (Xu *et al.*, 2018; Li *et al.*, 2020). Moreover, the total physical mass of the ring net and cables is assumed to be lumped over these nodal particles, according to which their density is adjusted (Dugelas *et al.*, 2019; Li *et al.*, 2020). The full model description (i.e. flexible barrier and key components), calibration and validation can be found in Li *et al.* (2020). Key parameters for the modelling of a flexible barrier are summarised in Table 1.

Within the same DEM framework, particle-wall interactions, in-flow interparticle interactions and interactions between barrier nodal particles and debris particles can all be readily handled. Meanwhile, the interaction between barrier nodal particles and debris fluid can be considered in the same manner as the fluid-particle interactions in a debris flow under the physics-based, unified CFD-DEM method. Thus, this study can model the loads of solid particles and the fluid in a debris flow being exerted on the barrier nodal particles by way of interparticle contact force and fluid-particle interaction force, respectively. Note that four fluid-particle interaction forces, namely, drag force, buoyancy force, viscous force and virtual mass force are considered in this work (Kong *et al.*, 2021a).

Model set-up and case plan

Figure 2 illustrates the model set-up for a solid-fluid mixture and a flexible barrier constructed on an inclined channel with a slope angle θ . The CFD domain is bounded by an upper atmosphere face, an outlet face at the end of the channel and four no-slip channel walls (Fig. 2(a)). In DEM,

Table 1. Key model parameters

Items	Properties	Values
Particle in a flow	Particle number	30 000
	Density*: kg/m ³	2500
	Diameter: m	0.04, 0.06 and 0.08
	Young's modulus (particle-particle contact): GPa	70
	Young's modulus (particle-wall contact): GPa	700
	Poisson's ratio*	0.3
	Restitution coefficient*	0.4
	Interparticle friction coefficient	0.7
	Particle-wall friction coefficient	0.5
	Rolling friction coefficient	0.15
	Particle in a barrier†	Diameter: m
Number		14 725
Density for ring element, cable, brake: kg/m ³		7800, 12 000, 20 000
Young's modulus: GPa		10
Poisson's ratio		0.3
Restitution coefficient		0.1
Friction coefficient		0.1
Bond in a barrier‡		Normal stiffness of ring element: N/m
	Shear stiffness of ring element: N/m	9×10^8
	Normal stiffness of cable: N/m	8×10^{11}
	Shear stiffness of cable: N/m	8×10^8
	Stiffnesses of the brake at stages 1 and 2: N/m	8×10^{11} , 8×10^{10}
	Activation force of the brake element: kN	2
Air*	Density: kg/m ³	1
	Viscosity: Pa s	1.48×10^{-5}
Fluid‡	Density: kg/m ³	1350
	Consistency index: Pa s ⁿ	21.30
	Flow index:	0.24
	Yield stress: Pa	17.86
Simulation control	Cell size in CFD: m	$0.15 \times 0.15 \times 0.15$
	Time step in DEM: s	5×10^{-7}
	Time step in CFD: s	5×10^{-6}
	Simulated real time: s	2–12

*Refer to typical values of physical properties for debris flows (Iverson, 1997).

†Refer to key parameters in the modelling of a flexible barrier (Xu *et al.*, 2018; Dugelas *et al.*, 2019; Li *et al.*, 2020).

‡Refer to typical values of the non-Newtonian fluids (Remaître *et al.*, 2005).

the sides and bottom of the flow channel are modelled as rigid walls with Young's modulus ten times that of the particles. The particle-wall sliding friction and rolling friction coefficients are set to 0.5 and 0.15, respectively. A mixture sample composed of tridisperse grains and viscous liquid (Fig. 2(b)) is initially assigned with prescribed velocities ($v_{\text{int}} = 2.2\text{--}7$ m/s) to flow down and impact the barrier. h_p , l_p and w_b are the height, length and width of the initial sample, respectively. The total volume and solid volume concentration for debris flows are 7.2 m³ and 0.5, respectively. The mass percentages of the particles with diameters d_p of 0.08 m, 0.06 m and 0.04 m are 70%, 15% and 15%, respectively. The total number of simulated particles in each simulation is 44 725 (30 000 in a flow and 14 725 in a barrier). Compared to water as the fluid phase (Shan & Zhao, 2014; Fang *et al.*, 2021), the viscous slurry in a debris flow is treated as a more complicated non-Newtonian fluid modelled with the Herschel-Bulkley model (Remaître *et al.*, 2005). Although debris flows cannot be accurately predicted by a fixed rheological formula (Major & Pierson, 1992; Iverson, 2003), the interstitial slurry fluid in a debris-flow mixture can be reasonably described by a Herschel-Bulkley model with shear-thinning rheology (Coussot *et al.*, 1998; Remaître *et al.*, 2005; Von Boetticher *et al.*, 2016). At the initial state, only fluid cells coinciding with the mixture sample portion are filled with liquid, and the rest of the CFD domain is filled with air. Key adopted parameters are summarised in Table 1.

To obtain a comprehensive understanding of the effects of the flow-barrier height ratio ε on the barrier load-deflection

behaviour, the ratio ε ranging from 0.1 to 1.0 is produced. It is wider than the measured values of ε (0.125 to 0.625) from field investigations by Wendeler *et al.* (2019). In this study, the large-scale ($10^0\text{--}10^1$ m) simulations, instead of real-scale ($10^1\text{--}10^3$ m) ones, are conducted for computational efficiency, and their dynamic similarity with real-scale geophysical flows is guaranteed by Froude similarity. The Froude similarity is commonly used in numerical and physical modelling for flow-structure interactions (Choi *et al.*, 2015; Wendeler *et al.*, 2019; Li *et al.*, 2021). Indeed, the Froude number has been widely used to characterise the flow dynamics in aiding the design of flow-resisting flexible barriers (Wendeler, 2016). It is defined as the ratio of the flow inertia to the external field due to gravity

$$\text{Fr} = v_0 / \sqrt{gh_0 \cos \theta} \quad (1)$$

where v_0 and g denote the average velocity of incoming flows and gravitational acceleration, respectively. Two test groups are generated: group I with varying v_{int} (2.2–7 m/s) and constant Fr (2.4), and group II with varying Fr (1.7–5.4) and constant v_{int} (5 m/s). The Fr value obtained is within the range measured from real debris flows, which is from 0.5 to 7.6 (Choi *et al.*, 2015). For convenient discussion, test IDs are defined according to group ID and the ratio ε . GI and GII denote groups I and II, respectively. Cases GIR20 and GIIR80 indicate the numerical tests of debris flows with $\varepsilon = 20\%$ in GI ($v_{\text{int}} = 3.1$ m/s, Fr = 2.4, Fig. 2(c), left-hand diagram) and $\varepsilon = 80\%$ in GII ($v_{\text{int}} = 5$ m/s, Fr = 5.4, Fig. 2(c), right-hand diagram), respectively. The test programme is

Table 2. Modelling programme

Groups	Properties	Values									
GI and GII	ε	0.1	0.2	0.3	0.4	0.5	0.6	0.7	0.8	0.9	1
	h_p : m	0.1	0.2	0.3	0.4	0.5	0.6	0.7	0.8	0.9	1
	l_p : m	40	20	13.3	10	8	6.7	5.7	5	4.4	4
GI	v_{int} : m/s	2.2	3.1	3.8	4.4	5	5.4	5.9	6.3	6.6	7.0
	Fr	2.4	2.4	2.4	2.4	2.4	2.4	2.4	2.4	2.4	2.4
GII	v_{int} : m/s	5	5	5	5	5	5	5	5	5	5
	Fr	5.4	3.8	3.1	2.7	2.4	2.2	2.1	1.9	1.8	1.7

summarised in Table 2. In addition to the flow–barrier height ratio and flow dynamics, the load–deflection behaviours of a flexible barrier can also be affected by other factors, including the specific barrier type and configuration and the incoming geophysical flow types. This study has adopted a fixed solid volume concentration of 0.5 as a demonstrative example to simulate a typical debris flow. In reality, the solid volume concentration typically ranges from 0.4 to 0.8 for debris flows (Iverson, 1997), and this factor can affect the mobility of debris flows and thus the impact mechanism against a flexible barrier (Song *et al.*, 2018; Kong *et al.*, 2021a).

For each case, the computational time on an eight-core Intel central processing unit (CPU) (3.7 GHz) desktop computer varies from 90 h to 390 h, depending on the targeted real time (2–12 s). Furthermore, the size of the simulated barrier is determined according to the scale of the set-up in Fig. 2(a). The barrier ring-net size (i.e. ring diameter equal to 70 mm) is determined to retain large particles in a flow while allowing small particles to pass through, which recovers the major function of a flexible barrier in reality. Note that the unresolved CFD–DEM approach employed in this study requires a maximum particle diameter smaller than the typical CFD cell size, and thereby it cannot fully resolve the detailed fluid motion around each particle (Kloss *et al.*, 2012; Zhao & Shan, 2013). The chosen size ratio of the fluid cell to the maximum or average particle diameter is considered reasonably accurate for solving the three-way flow–barrier interactions while maintaining affordable computational cost. Large-scale 3D simulations of debris flow against a flexible barrier using a fully resolved CFD–DEM method (Yu & Zhao, 2021) can help to provide more physical details, which can be explored in the future with further development of the coupled CFD–DEM method and an increase in computing power.

IMPACT DYNAMICS, LOAD COMPONENTS AND TRANSMISSIONS

Impact dynamics and load components

Figures 3(a) and 3(b) show the comparison of key flow–barrier interactions for flow-resisting flexible barriers observed between a large-scale flume test (25 m long, 2 m wide) performed by a reduced-scale flexible ring-net barrier (HKUST, 2019), and a representative numerical case GIR50 ($\varepsilon = 0.5$, $v_{int} = 5$ m/s, Fr = 2.4). Note that the green surface of the fluid visualises the contour surface with $\alpha_1 = 0.5$ (Fig. 3(b)). Three typical stages are identified, namely, frontal impact process (stage I), runup process (stage II) and overflow process (stage III). Experimental observations (Fig. 3(a)) witness a certain volume of the fluid and small particles passing through the barrier, which has been well captured by the numerical result (Fig. 3(b)).

Figure 3(c) shows the fluid–barrier interactions in terms of fluid volume fraction α_1 (streamlines) and fluid velocity

U^f (arrows). The velocity field of fluid is compounded and shown for better visualisation of dead zones (Faug, 2015; Kong *et al.*, 2021b) coexisting with the flowing layers. The boundaries of dead zones (dash-dotted lines in Figs 3(c) and 3(d)) are approximately determined based on a velocity threshold (i.e. below 5% of v_0) suggested by Faug *et al.* (2009). Moreover, the distribution density of streamlines indicates local flow discharge. The flows passing through the barrier rapidly decrease from $t = 0.25$ s to $t = 1$ s as the dead zone traps more solid particles, resulting in a low void ratio compared to flowing materials and thus a lower permeability.

Figure 3(d) demonstrates the solid–barrier interactions by the interparticle contact force (F^c) networks. The magnitude of F^c is denoted by the thickness of lines, where thick ones are strong contact forces and thin ones are weak contact forces. Strong force chains are observed at the bottom of the barrier at stage I and occur at both the lower and higher portions of the ramp-like dead zone at stages II and III (Fig. 3(d)). The dead zone is initially formed upstream of the barrier where the retained particles form a contact structure at stage II. More solid materials are then trapped in the dead zone, serving as a ramp surface for subsequent flows to override and eventually overflow the barrier at stage III.

Figure 3(e) illustrates the impact loading history with dynamic load F_b^{dyn} from flowing debris, the static load F_b^{sta} induced by dead zone and flowing layer, as well as the passive pressure F_b^{pas} and drag or shear force F_b^{dra} produced by the flowing or overtopping layer. Here, the macroscopic F_b can be cast as

$$F_b = F_b^{dyn} + F_b^{sta} + F_b^{pas} + F_b^{dra} \quad (2)$$

where the direct-impact induced force dominates at stage I while forces produced by the dead zone and flowing layer play substantial roles at stage III (Ashwood & Hungr, 2016). F_b^{dyn} , F_b^{pas} and F_b^{dra} can be transferred through the contact networks to the barrier (Fig. 3(d)). These difficult-to-estimate load components are crucial for evaluating impact loads on flow-resisting rigid and flexible barriers (Vagnon & Segalini, 2016; Albaba *et al.*, 2018; Tan *et al.*, 2020; Faug, 2021; Jiang *et al.*, 2021). In addition to well-explored factors (e.g. flow dynamics and components), the influences of ε on the relative dominance played by these forces at different stages will be discussed later.

Evolving load components and transmissions

Figure 4 presents time histories of impact load components and transmissions sustained by the barrier and cables in case GIR50. Both the solid and the fluid in impinging flows can exert impact forces on a flexible barrier and its cables, including solid–barrier contact force F_{s-b} , fluid–barrier interaction force F_{f-b} , solid–cable contact force F_{s-c} and fluid–cable interaction force F_{f-c} . The inset in Fig. 4(b) demonstrates typical forces acting on the nodal particle j in cable k . The interparticle bond force $F_b^{c,j}$ acting

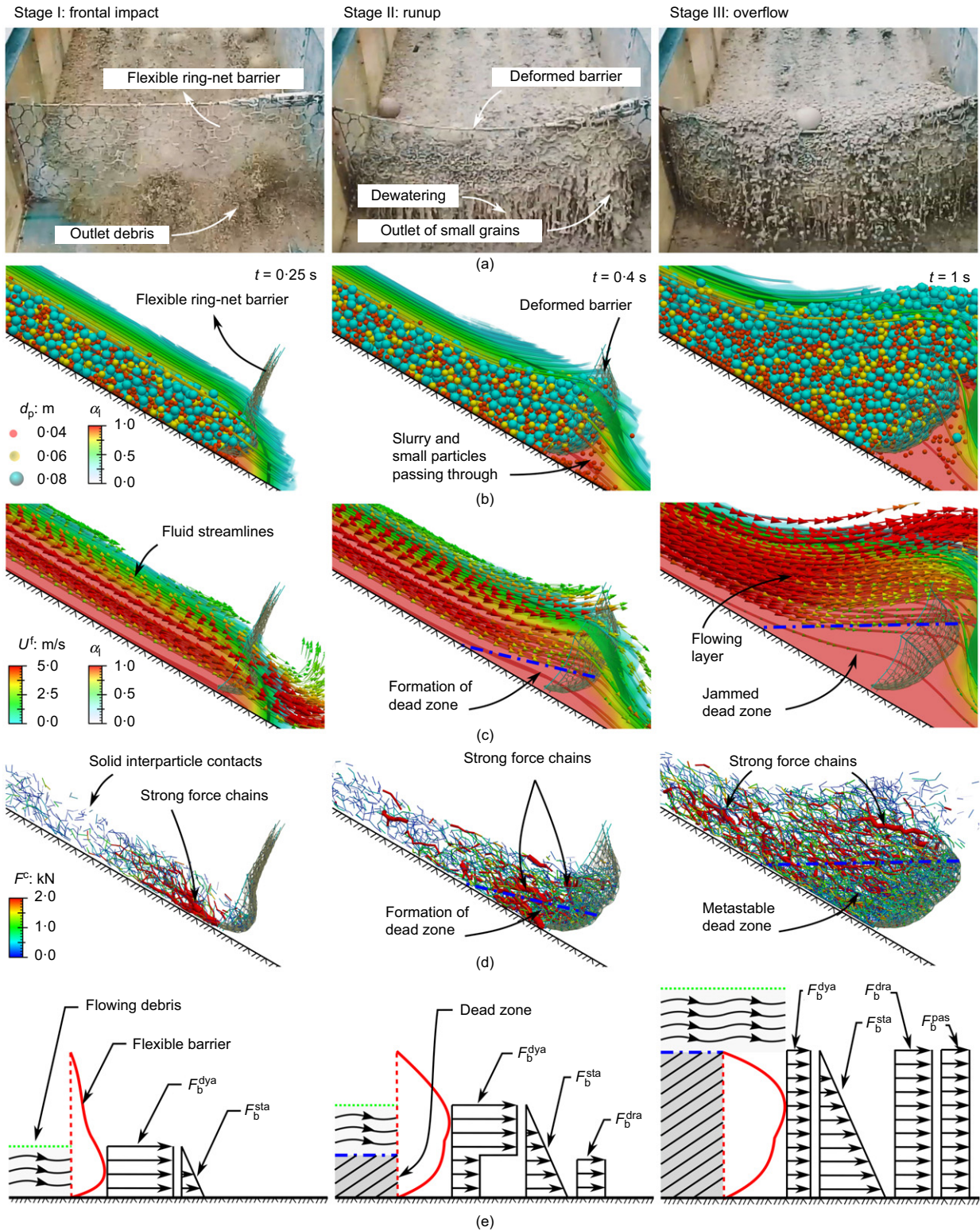


Fig. 3. Key flow-barrier interactions for debris flow impacting a flexible ring-net barrier: comparison between (a) experimental observations (HKUST, 2019) and (b) case GIR50; (c) fluid-barrier interactions; (d) solid-barrier interactions; and (e) sketches of the impact load components and history. A full-colour version of this figure can be found on the ICE Virtual Library (www.icevirtuallibrary.com)

on the cable nodal particle j is contributed by impinging flows (F_{s-c}^j and F_{f-c}^j), gravity F_g^j and the portion through in-barrier load transmission (ring-cable contact force F_{f-c}^j). Specifically, F_{s-c} is calculated by $F_{s-c} = \sum_{j \in n_k} F_{s-c}^j$ where n_k denotes the total number of nodal particles in cable k . Likewise, $F_{f-c} = \sum_{j \in n_k} F_{f-c}^j$; $F_{f-c} = \sum_{j \in n_k} F_{f-c}^j$. For the entire barrier, F_b is calculated by $F_b = \sum_{i \in n_b} F_{s-b}^i + \sum_{i \in n_b} F_{f-b}^i$ where n_b is the total number of nodal particles in the

barrier. $T = \text{Max}(F_b^{c,j})$ denotes the maximum tensile force in a cable.

Consequently, the employed fluid-solid approach enables physics-based measurement, which delineates the load components and transmissions. For instance, Fig. 4(a) shows that the maximum F_{s-b} (258 kN) is around ten times larger than the maximum F_{f-b} (24.5 kN, inset in Fig. 4(a)). This indicates that F_{s-b} is the dominant load contributor

to a flexible barrier, mainly resulting from high barrier permeability. Furthermore, $F_b^{Peak} = \text{Max}(F_b)$ occurs at stage III in case GIR50 (Fig. 4(a)), while impact stages I and II are commonly considered critical in predicting F_b^{Peak} for rigid countermeasures (Ng *et al.*, 2017; Song *et al.*, 2019). This finding implies the significance of considering

overtopping in the analysis and design of flexible barriers, especially for multi-level barriers.

Figures 4(b) and 4(c) show load components contributed by impinging flow (F_{s-c} and F_{f-c}) and those portions through in-barrier load transmission (F_{r-c} and T) for the middle and top cables, respectively. Note that the bottom cable is fixed to mimic the anchored boundaries in the field. F_{r-c} is the dominant contributor for T for cables since the developing trends of T generally coincide with F_{r-c} . Meanwhile, $\text{Max}(F_{r-c})$ values for both middle and top cables are around five times that of $\text{Max}(F_{s-c})$. This implies that cable force mainly results from ring-cable force sharing, rather than the direct debris-flow impact. During stages I and II, F_{s-c} , F_{r-c} and T in the middle cable show a sharp increasing-decreasing trend (Fig. 4(b)), while both F_{r-c} and T in the top cable increase continuously (Fig. 4(c)). The rapid increase of F_{r-c} and T in both cables indicates the effective force shearing of impact load induced by frontal and runoff impacts. The decrease of forces sustained by the middle cable is possibly caused by the formation of a dead zone at stage II, which diminishes the degree of direct debris-flow impacts. At the beginning of stage III, F_{s-c} , F_{r-c} and T in both cables indicate a quick increase until $t/t_0 \cong 0.25$ (Figs 4(b) and 4(c)). This is likely to be due to the increase of F_b^{sta} induced by the dead zone and more F_b^{pas} and F_b^{dra} produced by the overtopping flows. Therefore, the relative dominance played by the forces in equation (2) at different stages controls the evolving load distributions and transmissions among different barrier components. After $t/t_0 \cong 0.25$, forces sustained by cables experience a continuous decrease until $t/t_0 \cong 0.5$, owing to the lower kinetic energy carried by the subsequent tail flow and a progressive reduction of hydrostatic load induced by the drained debris cone. These forces tend to be stable as the trapped debris becomes stationary.

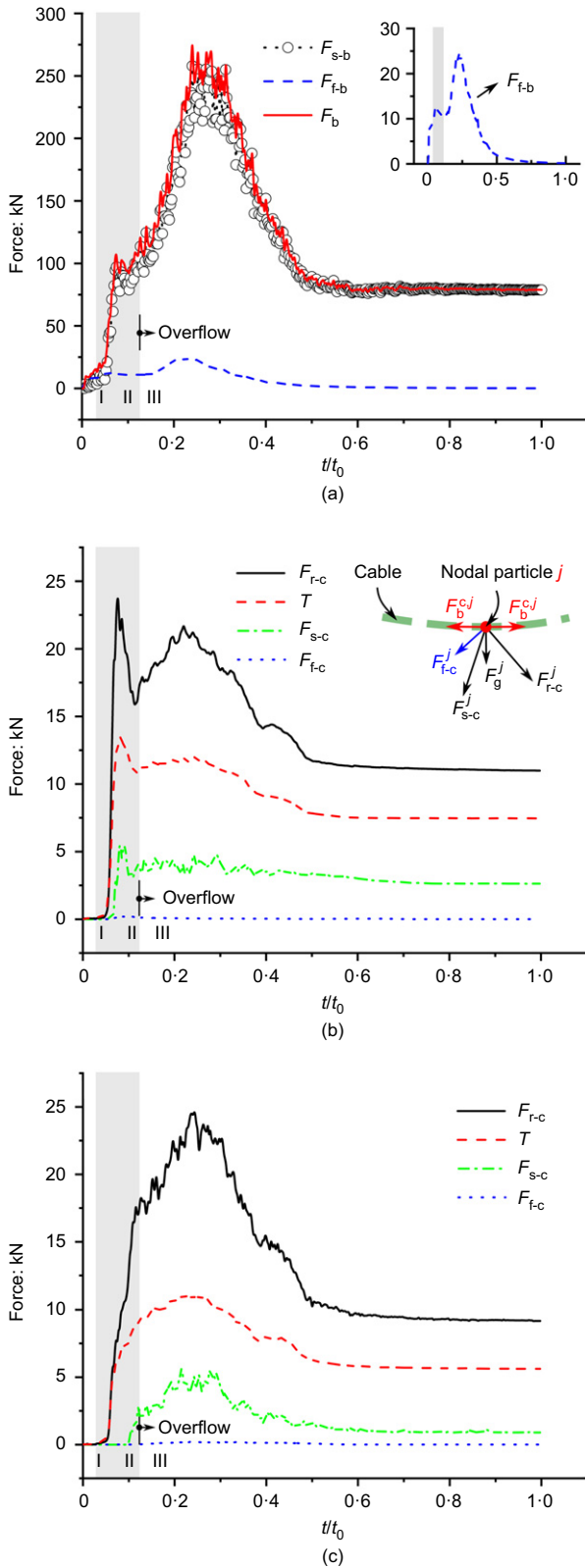


Fig. 4. Physics-based estimations of impact load components and transmissions sustained by (a) the flexible barrier and (b) middle and (c) top cables in GIR50 over time. The grey regions visualise stages I and II before overtopping

Flow-barrier height ratio compared against maximum cable force

Cable tensile forces are key data frequently measured in the field and in experiments (Bugnion *et al.*, 2012; Wendeler, 2016; Vicari *et al.*, 2022). Fig. 5 shows the influence of the ratio ϵ on $\text{Max}(T)$ sustained by both middle and top cables. v_{int} for cases in GI ($Fr = 2.4$) and Fr numbers for cases in GII ($v_{int} = 5 \text{ m/s}$) are listed in Table 2. A two-stage increase of $\text{Max}(T)$ with ϵ is observed. Specifically, the mean increasing rate of $\text{Max}(T)$ with ϵ is higher in the range of $\epsilon > 0.5$ than

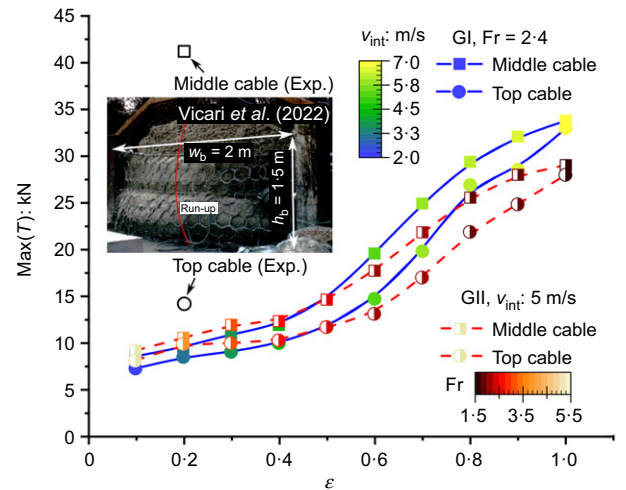


Fig. 5. The ϵ - $\text{Max}(T)$ relations for middle and top cables in both GI (solid symbols) and GII (half-empty symbols)

when $\varepsilon \leq 0.5$. Higher ε is likely to lead to reduced interaction duration before overtopping. Beyond a certain value of ε – that is $\varepsilon > 0.5$ in the present work – key flow–barrier interaction mechanisms (e.g. development of dead zone, barrier deformation behaviour) may change and hence result in different load–deflection behaviour to be examined later. For both cables, $\text{Max}(T)$ in GI is slightly smaller than that in GII when $\varepsilon \leq 0.4$, whereas it is bigger in GI than in GII when $\varepsilon \geq 0.6$ (Fig. 5). As expected, this transition occurs at around $\varepsilon = 0.5$, due primarily to the smaller v_{int} in GI than in GII when $\varepsilon \leq 0.4$ and bigger v_{int} in GI than in GII when $\varepsilon \geq 0.6$ (listed in Table 2). At the same ε , the increase of v_{int} indicates growth in both flow discharge and pre-impact kinetic energy, leading to more intense impacts and thus larger $\text{Max}(T)$. Moreover, $\text{Max}(T)$ sustained by the middle cable is always larger than that sustained by the top cable (Fig. 5). This implies that the middle cable is critical for supporting the barrier and should be a primary focus for practical design and analysis of flow-resisting flexible barriers.

Figure 5 presents valuable experimental data of $\text{Max}(T)$ (denoted by empty square and circle symbols) obtained from the large-scale flume (25 m long, 2 m wide) test V6-B1 ($\varepsilon = 0.2$, $v_0 = 6.1$ m/s, $\text{Fr} = 3.6$) on debris flow impacting a flexible barrier, as performed by Vicari *et al.* (2022), for comparison. The inset in Fig. 5 shows the reduced-scale flexible barrier (1.5 m high, 2 m wide) consisting of a ring net and top, middle and bottom cables equipped with brakes, which is overall consistent with the configuration of the numerical model (see Fig. 1(b)). Nonetheless, their barrier permeability is much smaller, resulting from the two-layered net: a reduced-size main ring net and a secondary fine wire mesh net (Vicari *et al.*, 2022). Consequently, even fine solids and slurry can hardly pass through the barrier (inset in Fig. 5). In addition, the height of the experimental barrier (1.5 m) is higher than the numerical model (0.9 m), resulting in more debris material being trapped. The two salient differences possibly contribute to the following discrepancies: (a) $\text{Max}(T)$ (41.5 kN) sustained by the middle cable in the experiment is much larger than the numerical prediction ($\text{Max}(T) = 10.6$ kN) under the same ratio ε (0.2) since the experiment adopts a higher, low-permeability barrier; (b) the difference of $\text{Max}(T)$ between the middle and top cables in the experiment is larger than the numerical results. This is because $\text{Max}(T)$ of the top cable usually occurs at a well-developed overflow process, while the experiment (Vicari *et al.*, 2022) only observed a single surge impact. In case GIR50 (see Figs 4(b) and 4(c)), $\text{Max}(T)$ from the middle cable occurs before overtopping, whereas $\text{Max}(T)$ in the top cable takes place at a well-developed overflow process when the forces induced by the flowing layer (F_b^{pas} and F_b^{dra}) play substantial roles. In addition, a lower barrier permeability in the experiment contributes to this discrepancy. $\text{Max}(T)$ values for the top and middle cables extracted from the experiment (Vicari *et al.*, 2022) are around 14.1 kN and 41.5 kN, respectively. In consideration of the above circumstances, their magnitudes are generally consistent with the numerical predictions of $\text{Max}(T)$ ranging from 7.2 kN to 33.8 kN.

ε -DEPENDENT LOAD-DEFLECTION MECHANISMS

Estimated non-linear load–deflection–stiffness relations

Figure 6 presents the ε -dependent load–deflection (F_b – D_h) relations of a flexible barrier in arresting debris flows. In reality, barrier deflection is a 3D phenomenon varying across both the width and height of a barrier, depending on the competitive roles of different load components in equation (2). The simple definitions of maximum barrier

deflection D_h and equivalent barrier stiffness k_b^n are highly idealised.

Figures 6(a) and 6(c) display the bi-linear, positive F_b – D_h relations in both GI and GII with $\varepsilon \leq 0.6$. This load–deflection mode comprises two major stages before the F_b^{Peak} : $k_{b,I}^n$ at the initial barrier deformation stage and $k_{b,II}^n$ at the following barrier deformation stage. Initially, $k_{b,I}^n$ is small under debris-flow impacts until D_h reaches the deflection point, since the entire barrier structure behaves rather flexibly. After the inflection point, the stiffness increases dramatically from $k_{b,I}^n$ to $k_{b,II}^n$, due to the exhaustion of flexible features of the barrier structure after most rings have deformed and the entire structure becomes progressively stiffer. Moreover, the ratio ε presents positive correlations with $k_{b,I}^n$, $k_{b,II}^n$, the maximum values of F_b and D_h , as well as D_h at the inflection point when $\varepsilon \leq 0.6$.

Beyond a certain value of ε – that is, $\varepsilon = 0.6$ in the present study – the development of F_b – D_h becomes much more complicated. For instance, $k_{b,I}^n$ in GI with $\varepsilon = 0.6$ presents an increasing–decreasing trend before the inflection point at $D_h = 0.45$ (Fig. 6(b)). Then F_b dramatically increases to F_b^{Peak} with an extremely large $k_{b,II}^n$ (~ 10 MN/m). A possible attribute lies in the faster formation of the dead zone and hence overtopping process with $\varepsilon = 0.6$ than with smaller ε . A similar trend is also observed in GII with $\varepsilon = 0.6$ (Fig. 6(d)). Therefore, $k_{b,I}^n$ in case GIR60 is approximately measured for simplicity. Moreover, Figs 6(b) and 6(d) show that $k_{b,I}^n$ is rather close to $k_{b,II}^n$ with $0.7 \leq \varepsilon \leq 0.9$, while $k_{b,I}^n$ dramatically decreases to a marginally small value with $\varepsilon = 1$, which is even smaller than the cases with $\varepsilon = 0.1$. The flow–barrier interactions will present a distinct behaviour when the flow thickness reaches the barrier height. It is likely for this reason that the overtopping can occur instantly and a dead zone is formed synchronously when $\varepsilon = 1$.

Interestingly, the backward and forward lines with arrows in Fig. 6 indicate two opposite developing trends of D_h after the peak F_b within a certain duration: shrinkage and expansion. This implies that D_h will begin to decrease after F_b^{Peak} (shrinkages with $\varepsilon \leq 0.6$) or continuously increase (expansions with $\varepsilon \geq 0.7$). The post-peak barrier expansion is likely to be caused by the combined effects of the trends that the interaction duration before overtopping is shorter, the downward load and deformation become more important, and forces induced by the overtopping layer are greater for cases when $\varepsilon \geq 0.7$. For instance, the insets in Figs 6(a) and 6(d) present two snapshots at F_b^{Peak} from GIR50 ($\varepsilon = 0.5$, $\text{Fr} = 2.4$) and GIIR100 ($\varepsilon = 1$, $\text{Fr} = 1.7$) with the same v_{int} (5 m/s), respectively. The F_b^{Peak} occurs at a well-developed overflow process with $\varepsilon = 0.5$, while it takes place at the initial stage of overtopping with $\varepsilon = 1$. Larger ε produces greater F_b^{pas} and F_b^{dra} from the overtopping layer, which contributes to the forward barrier deflection more than the dead zone induced F_b^{sta} . It is anticipated that the two forces in GIIR100 will further increase after F_b^{Peak} despite the decrease of F_b . To the best of the authors' knowledge, there remains no experimental observation or theoretical analysis of this interesting phenomenon. However, estimation of debris-flow impacts on a flexible barrier is challenging, as it is not directly measurable in experiments or fields (Wendeler, 2016; Ng *et al.*, 2017). In contrast, the post-peak barrier shrinkage is mainly due to the sharp decrease of F_b that cannot maintain the excessive deformation of the barrier. Notably, barrier shrinkage has been observed by large-scale flume tests conducted (DeNatale *et al.*, 1999).

Three ε -dependent load–deflection modes

Based on representative cases with ε equal to 0.4, 0.8 and 1 in GII (Figs 6(c) and 6(d)), three generalised modes of the

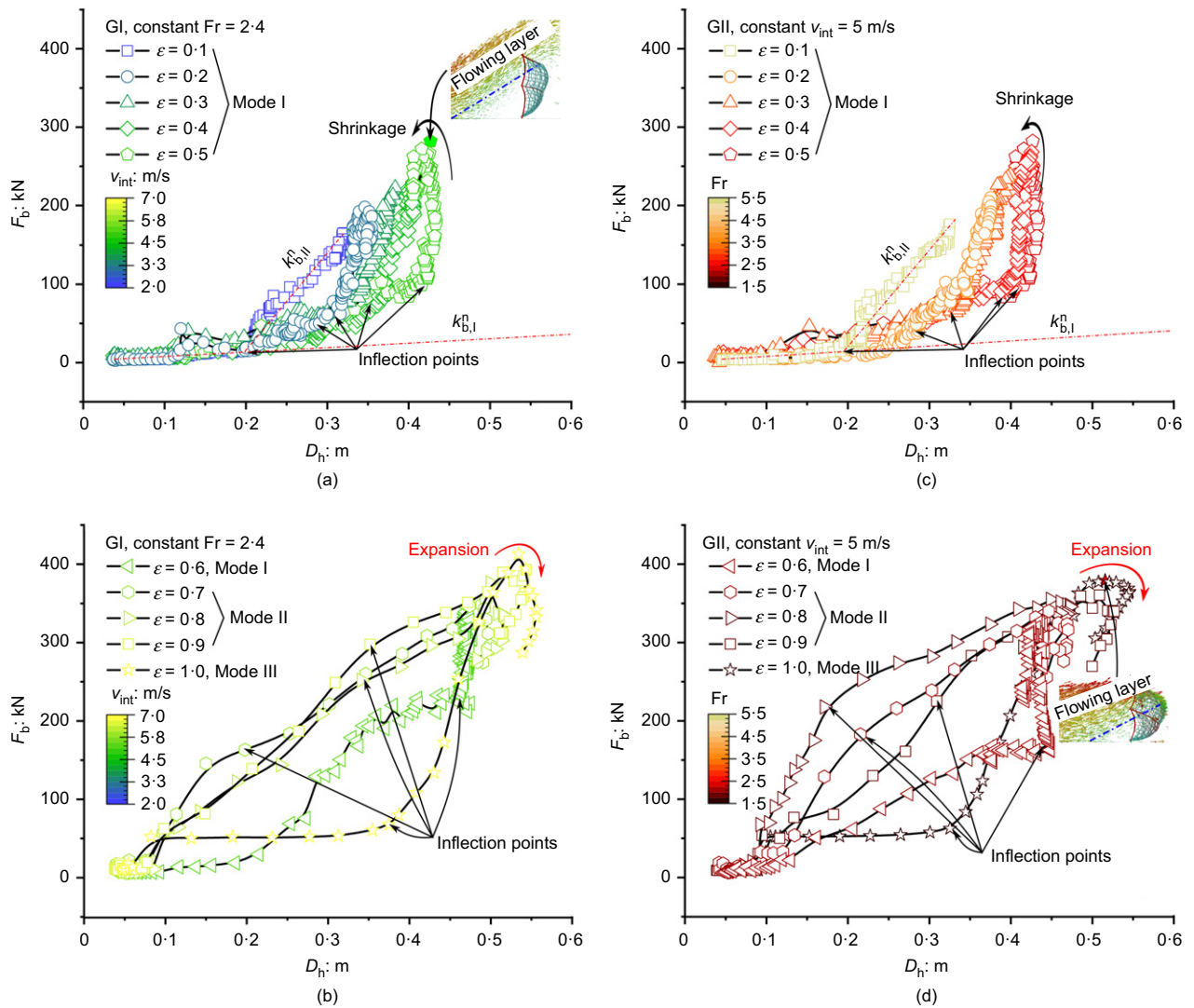


Fig. 6. The ϵ -dependent load–deflection (F_b – D_h) relations in both (a), (b) GI and (c), (d) GII. The insets in (a) and (d) are snapshots at F_b^{Peak} from cases GIR50 and GIIR100, respectively

ϵ -dependent F_b – D_h relations are further examined in Fig. 7(a). Their key estimated determining parameters are crucial factors for developing analytical impact models and engineering designs, including $k_{b,I}^n$ and $k_{b,II}^n$, the normalised maximum barrier deflection $\text{Max}(D_h)/(\bar{W}_b/2)$ and F_b^{Peak} presented in Figs 7(b), 7(c) and 7(d), respectively. According to the ratio ϵ of a case, v_{int} for a case in GI ($Fr = 2.4$) and Fr number for a case in GII ($v_{\text{int}} = 5 \text{ m/s}$) can be found in Table 2. Note that big boulders commonly observed in natural debris flows (Iverson *et al.*, 2011; Ng *et al.*, 2021) can produce brief but much higher peak impacts and generate destructive responses to a flexible barrier. This critical aspect will be explored in the future. The three generalised modes and their determining parameters presented in Fig. 7 are only applicable to debris flows with continuous and distributed loading characteristics.

As illustrated in Fig. 7(a), the load–deflection mode I (solid line) with $\epsilon \leq 0.6$ has two distinctive characteristics: $k_{b,I}^n$ at the initial barrier deformation stage being significantly smaller than $k_{b,II}^n$ at the following barrier deformation stage and the post-peak barrier shrinkage. Notably, mode I should be critical in the design of flow-resisting flexible barriers since field measured ϵ ranges from 0.125 to 0.625 (Wendeler *et al.*, 2019). Mode II (black dotted line) is simplified from a much more complicated F_b – D_h relations with $0.7 \leq \epsilon \leq 0.9$, where

$k_{b,I}^n$ is close to $k_{b,II}^n$ or even larger than $k_{b,II}^n$ and the post-peak barrier expansion is observed. Furthermore, key features of mode III with $\epsilon \sim 1$ (dashed line) include $k_{b,I}^n$ being significantly smaller than $k_{b,II}^n$ and the post-peak barrier expansion.

Moreover, the shaded areas for the three load–deflection modes (Fig. 7(a)) indicate the strain energy stored by the flexible barrier to a certain extent. Conceptually, assuming the linear increase of F_b , plotted against the deformation D_h , produces the strain energy of the barrier at F_b^{Peak} . By comparing the shaded areas before F_b^{Peak} for three modes (i.e. mode II > mode I or mode III), a flexible barrier can store more impact energy from impinging flows with $0.7 \leq \epsilon \leq 0.9$ than $\epsilon \leq 0.6$ or $\epsilon \leq 1$. This implies that the structural deformability of flexible barriers in dissipating impact energy and thus attenuating the peak impact load can be utilised to the best advantage subjected to impinging flows with $0.7 \leq \epsilon \leq 0.9$. In reality, the energy-sinking flow–barrier interactions involve complex energy dissipation and transformation in impinging flows (e.g. viscous shearing, frictional sliding and collision in both flowing layer and dead zone) and by the barrier (e.g. barrier deformation, frictional sliding and energy dissipator). Therefore, quantitative examinations of the F_b – D_h relations may provide a new way to quantify the barrier strain energy for possibly improving the understanding of the entire energy-sinking process.

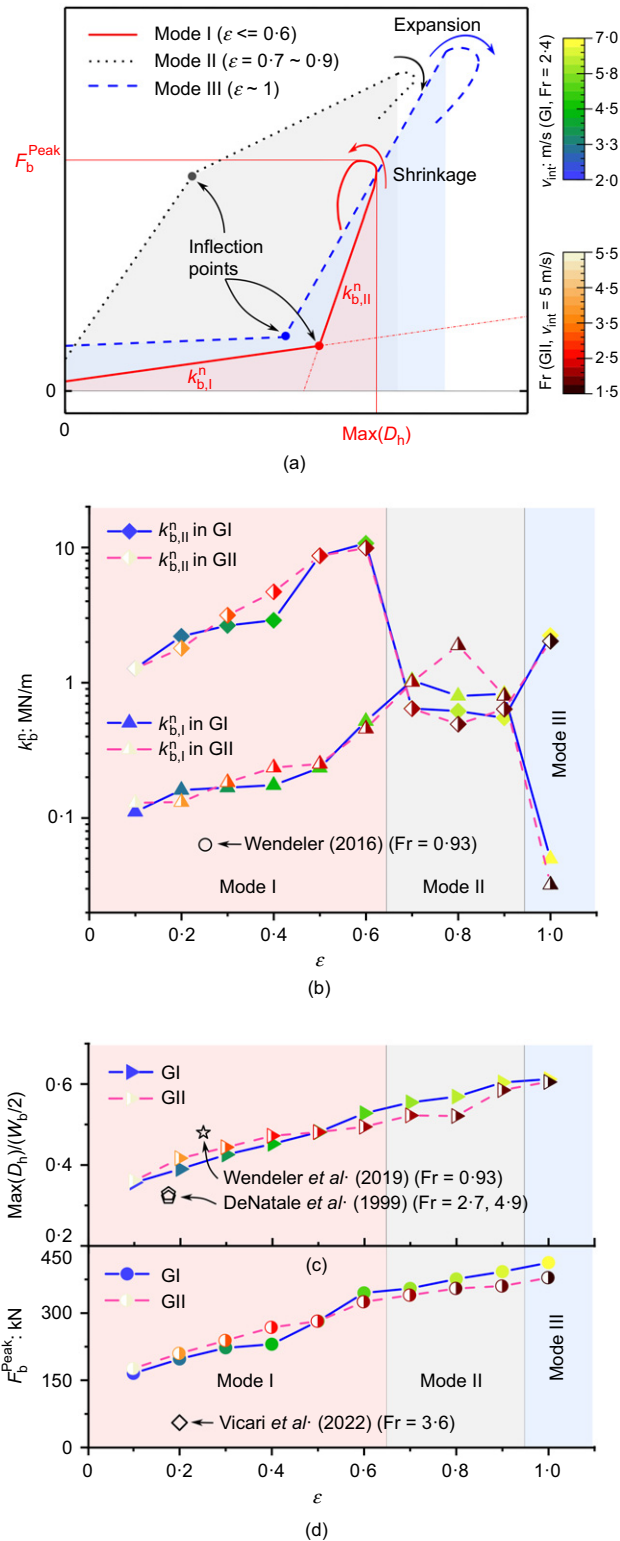


Fig. 7. (a) Three ε -dependent load-deflection (F_b - D_h) modes and (b)-(d) their estimated key determining parameters of a flexible ring-net barrier in mitigating debris flows

Figure 7(b) shows the effect of ε on stiffnesses $k_{b,I}^n$ and $k_{b,II}^n$. The ratio ε shows a positive correlation with $k_{b,I}^n$ and $k_{b,II}^n$ under mode I, wherein $k_{b,I}^n$ is much lower than $k_{b,II}^n$. As ε increases from 0.1 to 0.6, $k_{b,II}^n$ increases dramatically from 1.2 MN/m to 10 MN/m, whereas $k_{b,I}^n$ only increases from 0.15 MN/m to 0.55 MN/m. Based on the back-calculation of debris-flow event data, Wendeler (2016) calculated $k_b^n = 0.063$ MN/m (empty black circle) according

to the Timoshenko beam theory. Wendeler (2016) also reported a continually decreasing trend of k_b^n with D_h based on the conservation of energy, which ignores the possible energy losses occurring and outlet materials. Notably, Song *et al.* (2019) reported that barrier stiffness at the initial deformation stage was larger than at the following stage with an impermeable barrier made by membrane and cables. Nonetheless, the numerical results indicate that $k_{b,I}^n$ is much lower than $k_{b,II}^n$ with $\varepsilon \leq 0.6$ (Fig. 7(b)). It is conceivable that the initial barrier deformation process with $k_{b,I}^n$ is dominated by the inherent flexible features of the barrier instead of flow dynamics (ε and v_0) when the barrier behaves flexibly. Meanwhile, a stiffer flexible barrier at the subsequent deformation process results in more dramatic and much faster flow-barrier interactions with a larger ε . Moreover, with increasing ε , $k_{b,I}^n$ presents a sharp increase before dropping, whereas $k_{b,II}^n$ experiences a decrease before increasing, when $\varepsilon > 0.6$ (Fig. 7(b)). As discussed in the previous section, the flow-barrier interactions show distinct features when $\varepsilon \geq 0.6$. Despite v_{int} or Fr changing in GI or GII, the developing trends of ε - $k_{b,I}^n$ or ε - $k_{b,II}^n$ are quite consistent, indicating that ε can dominate barrier deformation characteristics compared with either Fr or v_{int} of anticipated flows.

Figures 7(c) and 7(d) show that both $Max(D_h)/(W_b/2)$ and F_b^{Peak} are strongly, positively correlated with ε , despite the decrease of Fr with the growth of ε in GII. It is evidenced that ε can strongly affect both $Max(D_h)$ and F_b^{Peak} more than Fr . Consequently, the widely adopted Fr -based empirical coefficients used in various analytical impact models for flexible barriers (Kwan & Cheung, 2012; Wendeler, 2016) may provide unreasonable predictions. Thus, the ratio ε is recommended to be explicitly considered in analytical impact models and engineering designs for flow-resisting flexible barriers.

Figure 7(c) shows that $Max(D_h)/(W_b/2)$ obtained from both the field (Wendeler *et al.*, 2019) and the numerical predictions are larger than that extracted from experiments (DeNatale *et al.*, 1999). This is likely to be because no overtopping was observed in experiments (DeNatale *et al.*, 1999). Moreover, Vicari *et al.* (2022) reported $F_b^{Peak} = 55$ kN based on the large-scale flume test (inset in Fig. 5), which is significantly lower than numerical predictions under similar Fr or ε conditions (Fig. 7(d)). This is antithetical to expectation since the experiment adopts a higher and low-permeability flexible barrier, and the measured $Max(T)$ of the middle cable is much larger than the numerical results (see Fig. 5). Vicari *et al.* (2022) calculated F_b^{Peak} according to a widely adopted simplified solution originally proposed by Ng *et al.* (2017), which mainly involves cable load and deformed angles. The numerical results imply that this cable-based simplified solution may underestimate F_b^{Peak} for flow-resisting flexible barriers. Therefore, it remains critical to evaluate whether the various simplified solutions in measuring debris-flow impacts on flexible barriers (e.g. Ng *et al.*, 2017; Tan *et al.*, 2019; Song *et al.*, 2022) give consistent, accurate predictions on the impact process. They also need to be further scrutinised – for example, by proper physical tests – to assess their validity in predicting the inter-twined relations among impinging flow properties, cable force, barrier deformation and barrier load.

CONCLUSIONS

This study has numerically examined the intricate load-deflection relations of a flexible ring-net barrier in arresting two-phase debris flows. A coupled CFD-DEM was employed to model the complicated multi-way, multi-phase interactions among the debris particles, debris fluid and all constituent barrier components. It was demonstrated that the method employed enables a unified consideration of essential

physics involved in the impact process, such as cable–ring–ring frictional sliding, dewatering and small particles passing through. Numerical predictions of key flow–barrier interactions and cable forces show reasonable consistency with large-scale experiments. The main findings and perspectives are summarised as follows.

- (a) This work enables physics-based estimation of debris-flow load on a flexible barrier that delineates the contributions of debris–solid and debris–fluid to the total impact load acting on the barrier and its components, providing quantitative investigations on evolving load sharing and transfer mechanisms. The results highlight the overtopping process and the solid–barrier contact force being the dominant load contributor to a flexible barrier. Cables act as major load bearers, and their locations significantly differentiate their roles in load carrying. The collective ring–cable contact forces control the cable tensile force, serving as a key mechanism for effectively transferring debris impact loads received by individual rings. Moreover, the competitive roles of macroscopic load components from the dead zone and flowing layer at different stages drive the characteristics of load distribution and transmission, and the prevailing load–deflection behaviour.
- (b) A diagram was obtained first to uncover the flow–barrier height ratio ε -dependent relations among barrier deflection, impact load and equivalent barrier stiffness, and its novelty is four-fold. (i) The ratio ε bears strong, positive correlations with the peak values of impact load and barrier deflection, which are key parameters for engineering designs. In addition to Fr, the ratio ε is recommended to be explicitly considered in analytical impact models and engineering designs for flexible barriers. (ii) The bi-linear, positive load–deflection relations before the peak barrier load are observed with $\varepsilon \leq 0.6$, wherein equivalent barrier stiffness $k_{b,I}^n$ at initial barrier deformation stage is significantly smaller than $k_{b,II}^n$ at the subsequent stage. (iii) The post-peak barrier deformation experiences a shrinkage with $\varepsilon \leq 0.6$ and expansion under $\varepsilon > 0.6$. This is possibly controlled by the competitive roles of different load components acting on the barrier, which can be significantly affected by ε . (iv) Three ε -dependent load–deflection modes and estimated determining parameters have been clarified for the first time; this clarification gives deep insights into the barrier load–deflection mechanisms and provides crucial information for practical flexible barrier design.

ACKNOWLEDGEMENTS

The research reported in this study was financially supported by the National Natural Science Foundation of China (projects #11972030 and #51909227) and the University Grants Council of Hong Kong (RGC/GRF projects #16205418, #27202419).

NOTATION

D_h	maximum barrier deflection parallel to the flow direction
d_p	diameter of particles
F_b, F_b^{Peak}	normal impact load and maximum normal impact load on a barrier
$F_b^{\text{dra}}, F_b^{\text{pas}}$	drag force and passive pressure produced by a flowing layer
$F_b^{\text{dyn}}, F_b^{\text{sta}}$	dynamic load from impinging flow and static load induced by a dead zone

F^c, F_b^c	interparticle contact force and interparticle bond force in a flexible barrier
\bar{F}^n, \bar{F}^s	axial and shear-directed forces
Fr	Froude number
F_{s-b}, F_{f-b}	solid–barrier contact and fluid–barrier interaction force
$F_{s-c}, F_{f-c}, F_{r-c}$	solid–cable contact, fluid–cable interaction and ring–cable contact forces
g	magnitude of gravitational acceleration vector
h_0, h_b, w_b	height of incoming flow front, height and width of a flexible barrier
h_p, l_p	height and length of the initial sample
$k_b^n, k_{b,I}^n, k_{b,II}^n$	equivalent barrier stiffness, equivalent barrier stiffnesses at the initial barrier deformation stage and the subsequent barrier deformation stage
\bar{k}^n, \bar{k}^s	normal and shear stiffnesses per unit area
\bar{M}^n, \bar{M}^s	axial and shear-directed moments
n_b, n_k	total number of nodal particles in a flexible barrier and the cable k
\bar{R}_{AB}, R_A, R_B	radii of a parallel bond, connected particles A and B
T	maximum tensile force in a cable
U^f	averaged velocity for the fluid in a cell
v_0, v_{int}	averaged velocity of incoming flow front and initial velocity of a flow sample
x, y, z	coordinate axes
α_1	liquid volume fraction
ε	flow–barrier height ratio
θ	slope angle
$\bar{\lambda}$	bond-radius multiplier
$\bar{\sigma}_c, \bar{\tau}_c$	tensile and shear strengths of a parallel bond

REFERENCES

- Albaba, A., Lambert, S., Kneib, F., Chareyre, B. & Nicot, F. (2017). DEM modeling of a flexible barrier impacted by a dry granular flow. *Rock Mech. Rock Engng* **50**, No. 11, 3029–3048, <https://doi.org/10.1007/s00603-017-1286-z>.
- Albaba, A., Lambert, S. & Faug, T. (2018). Dry granular avalanche impact force on a rigid wall: analytic shock solution versus discrete element simulations. *Phys. Rev. E* **97**, No. 5, 052903, <https://doi.org/10.1103/PhysRevE.97.052903>.
- Ashwood, W. & Hungri, O. (2016). Estimating total resisting force in flexible barrier impacted by a granular avalanche using physical and numerical modeling. *Can. Geotech. J.* **53**, No. 10, 1700–1717, <https://doi.org/10.1139/cgj-2015-0481>.
- Brighenti, R., Segalini, A. & Ferrero, A. M. (2013). Debris flow hazard mitigation: a simplified analytical model for the design of flexible barriers. *Comput. Geotech.* **54**, 1–15, <https://doi.org/10.1016/j.compgeo.2013.05.010>.
- Bugnion, L., McArdell, B. W., Bartelt, P. & Wendeler, C. (2012). Measurements of hillslope debris flow impact pressure on obstacles. *Landslides* **9**, No. 2, 179–187, <https://doi.org/10.1007/s10346-011-0294-4>.
- Bui, H. H. & Nguyen, G. D. (2021). Smoothed particle hydrodynamics (SPH) and its applications in geomechanics: from solid fracture to granular behaviour and multiphase flows in porous media. *Comput. Geotech.* **138**, 104315, <https://doi.org/10.1016/j.compgeo.2021.104315>.
- Choi, C. E., Ng, C. W. W., Au-Yeung, S. C. H. & Goodwin, G. R. (2015). Froude characteristics of both dense granular and water flows in flume modelling. *Landslides* **12**, No. 6, 1197–1206, <https://doi.org/10.1007/s10346-015-0628-8>.
- Coulbaly, J. B., Chanut, M. A., Lambert, S. & Nicot, F. (2018). Sliding cable modeling: an attempt at a unified formulation. *Int. J. Solids Structs* **130**, 1–10, <https://doi.org/10.1016/j.ijsolstr.2017.10.025>.
- Coussot, P., Laigle, D., Aratano, M., Deganuttill, A. & Marchi, L. (1998). Direct determination of rheological characteristics of debris flow. *J. Hydraul. Engng* **124**, No. 8, 865–868, [https://doi.org/10.1061/\(ASCE\)0733-9429\(1998\)124:8\(865\)](https://doi.org/10.1061/(ASCE)0733-9429(1998)124:8(865)).
- DeNatale, J. S., Iverson, R. M., Major, J. J., LaHusen, R. G., Fiegel, G. L. & Duffy, J. D. (1999). Experimental testing of flexible barriers for containment of debris flows, US

- Geological Survey Open-File Report 99-205, <https://doi.org/10.3133/OFR99205>. Vancouver, WA, USA: US Department of the Interior, US Geological Survey.
- Dugelas, L., Coulibaly, J. B., Bourrier, F., Lambert, S., Chanut, M. A., Olmedo, I. & Nicot, F. (2019). Assessment of the predictive capabilities of discrete element models for flexible rockfall barriers. *Int. J. Impact Engng* **133**, 103365, <https://doi.org/10.1016/j.ijimpeng.2019.103365>.
- EOTA (European Organization for Technical Assessment) (2016). *Flexible kits for retaining debris flows and shallow landslides/open hill debris flows*, European Assessment Document EAD 340020-00-0106. Brussels, Belgium: European Organization for Technical Assessment. See <https://www.nlfnorm.cz/en/ehn/6329#> (accessed 03/01/2023).
- Fang, J., Wang, L., Hong, Y. & Zhao, J. (2021). Influence of solid–fluid interaction on impact dynamics against rigid barrier: CFD–DEM modelling. *Géotechnique* **72**, No. 5, 391–406, <https://doi.org/10.1680/jgeot.19.P160>.
- Faug, T. (2015). Depth-averaged analytic solutions for free-surface granular flows impacting rigid walls down inclines. *Phys. Rev. E* **92**, No. 6, 062310, <https://doi.org/10.1103/PhysRevE.92.062310>.
- Faug, T. (2021). Impact force of granular flows on walls normal to the bottom: slow versus fast impact dynamics. *Can. Geotech. J.* **58**, No. 1, 114–124, <https://doi.org/10.1139/cgj-2019-0399>.
- Faug, T., Beguin, R. & Chanut, B. (2009). Mean steady granular force on a wall overflown by free-surface gravity-driven dense flows. *Phys. Rev. E* **80**, No. 2, 021305, <https://doi.org/10.1103/PhysRevE.80.021305>.
- Fávero Neto, A. H., Askarinejad, A., Springman, S. M. & Borja, R. I. (2020). Simulation of debris flow on an instrumented test slope using an updated Lagrangian continuum particle method. *Acta Geotech.* **15**, No. 10, 2757–2777, <https://doi.org/10.1007/s11440-020-00957-1>.
- Ferrero, A. M., Segalini, A. & Umili, G. (2015). Experimental tests for the application of an analytical model for flexible debris flow barrier design. *Engng Geol.* **185**, 33–42, <https://doi.org/10.1016/j.enggeo.2014.12.002>.
- GEOVERT (2016). *Geohazard mitigation: Shenandoah debris flow barrier*. Auckland, New Zealand: GEOVERT. See <https://www.geovert.com/gedp-past-projects/Shenandoah/Debris-Flow-Barrier> (accessed 05/11/2022).
- Hákonardóttir, K. M., Hogg, A. J., Batey, J. & Woods, A. W. (2003). Flying avalanches. *Geophys. Res. Lett.* **30**, No. 23, 2191, <https://doi.org/10.1029/2003GL018172>.
- HKUST (Hong Kong University of Science and Technology) (2019). HKUST. *YouTube*, 6 June. See <https://www.youtube.com/watch?v=wjTjQGMfgpU&list.html> (accessed 05/11/2022).
- Hoch, O. J., McGuire, L. A., Youberg, A. M. & Rengers, F. K. (2021). Hydrogeomorphic recovery and temporal changes in rainfall thresholds for debris flows following wildfire. *J. Geophys. Res. Earth Surf.* **126**, No. 12, e2021JF006374, <https://doi.org/10.1029/2021JF006374>.
- Iverson, R. M. (1997). The physics of debris flows. *Rev. Geophys.* **35**, No. 3, 245–296, <https://doi.org/10.1029/97RG00426>.
- Iverson, R. M. (2003). The debris-flow rheology myth. In *Debris-flow hazards mitigation: mechanics, prediction, and assessment* (eds D. Rickenmann and C. L. Chen), vol. 1, pp. 303–314. Rotterdam, the Netherlands: Millpress.
- Iverson, R. M., Reid, M. E., Logan, M., LaHusen, R. G., Godt, J. W. & Griswold, J. P. (2011). Positive feedback and momentum growth during debris-flow entrainment of wet bed sediment. *Nature Geosci.* **4**, No. 2, 116–121, <https://doi.org/10.1038/ngeo1040>.
- Jiang, Y. J., Fan, X. Y., Su, L. J., Xiao, S. Y., Sui, J., Zhang, R. X., Song, Y. & Shen, Z. W. (2021). Experimental validation of a new semi-empirical impact force model of the dry granular flow impact against a rigid barrier. *Landslides* **18**, No. 4, 1387–1402, <https://doi.org/10.1007/s10346-020-01555-8>.
- Kloss, C., Goniva, C., Hager, A., Amberger, S. & Pirker, S. (2012). Models, algorithms and validation for opensource DEM and CFD–DEM. *Prog. Comput. Fluid Dyn.* **11**, No. 2/3, 140–152, <https://doi.org/10.1504/PCFD.2012.047457>.
- Kong, Y., Li, X. & Zhao, J. (2021a). Quantifying the transition of impact mechanisms of geophysical flows against flexible barrier. *Engng Geol.* **289**, 106188, <https://doi.org/10.1016/j.enggeo.2021.106188>.
- Kong, Y., Zhao, J. & Li, X. (2021b). Hydrodynamic dead zone in multiphase geophysical flows impacting a rigid obstacle. *Powder Technol.* **386**, 335–349, <https://doi.org/10.1016/j.powtec.2021.03.053>.
- Kwan, J. S. H. & Cheung, R. W. M. (2012). *Suggestion on design approaches for flexible debris-resisting barriers*. Discussion Note DN1/2012. Hong Kong, China: The Government of Hong Kong Standards and Testing Division.
- Leonardi, A., Wittel, F. K., Mendoza, M., Vetter, R. & Herrmann, H. J. (2016). Particle–fluid–structure interaction for debris flow impact on flexible barriers. *Comput.-Aided Civ. Infrastruct. Engng* **31**, No. 5, 323–333, <https://doi.org/10.1111/mice.12165>.
- Li, X. & Zhao, J. (2018). Dam-break of mixtures consisting of non-Newtonian liquids and granular particles. *Powder Technol.* **338**, 493–505, <https://doi.org/10.1016/j.powtec.2018.07.021>.
- Li, X., Zhao, J. & Kwan, J. S. (2020). Assessing debris flow impact on flexible ring net barrier: a coupled CFD–DEM study. *Comput. Geotech.* **128**, 103850, <https://doi.org/10.1016/j.compgeo.2020.103850>.
- Li, X., Zhao, J. & Soga, K. (2021). A new physically based impact model for debris flow. *Géotechnique* **71**, No. 8, 674–685, <https://doi.org/10.1680/jgeot.18.P365>.
- Li, D., Lu, X., Walling, D. E., Zhang, T., Steiner, J. F., Wasson, R. J., Harrison, S., Nepal, S., Nie, Y., Immerzeel, W. W., Shugar, D. H., Koppes, M., Lane, S., Zeng, Z., Sun, X., Yegorov, A. & Bolch, T. (2022). High Mountain Asia hydropower systems threatened by climate-driven landscape instability. *Nature Geosci.* **15**, No. 7, 520–530, <https://doi.org/10.1038/s41561-022-00953-y>.
- Liu, C., Yu, Z. & Zhao, S. (2020). Quantifying the impact of a debris avalanche against a flexible barrier by coupled DEM–FEM analyses. *Landslides* **17**, No. 1, 33–47, <https://doi.org/10.1007/s10346-019-01267-8>.
- Major, J. J. & Pierson, T. C. (1992). Debris flow rheology: experimental analysis of fine-grained slurries. *Water Resour. Res.* **28**, No. 3, 841–857, <https://doi.org/10.1029/91WR02834>.
- Marchelli, M., Leonardi, A., Pirulli, M. & Scavia, C. (2020). On the efficiency of slit-check dams in retaining granular flows. *Géotechnique* **70**, No. 3, 226–237, <https://doi.org/10.1680/jgeot.18.P044>.
- Ng, C. W. W., Song, D., Choi, C. E., Liu, L. H. D., Kwan, J. S. H., Koo, R. C. H. & Pun, W. K. (2017). Impact mechanisms of granular and viscous flows on rigid and flexible barriers. *Can. Geotech. J.* **54**, No. 2, 188–206, <https://doi.org/10.1139/cgj-2016-0128>.
- Ng, C. W. W., Choi, C. E., Koo, R. C. H., Goodwin, G. R., Song, D. & Kwan, J. S. (2018). Dry granular flow interaction with dual-barrier systems. *Géotechnique* **68**, No. 5, 386–399, <https://doi.org/10.1680/jgeot.16.P273>.
- Ng, C. W. W., Wang, C., Choi, C. E., De Silva, W. A. R. K. & Poudyal, S. (2020). Effects of barrier deformability on load reduction and energy dissipation of granular flow impact. *Comput. Geotech.* **121**, 103445, <https://doi.org/10.1016/j.compgeo.2020.103445>.
- Ng, C. W. W., Liu, H., Choi, C. E., Kwan, J. S. & Pun, W. K. (2021). Impact dynamics of boulder-enriched debris flow on a rigid barrier. *J. Geotech. Geoenviron. Engng* **147**, No. 3, 04021004, [https://doi.org/10.1061/\(ASCE\)GT.1943-5606.0002485](https://doi.org/10.1061/(ASCE)GT.1943-5606.0002485).
- Pisano, L., Zumpano, V., Malek, Ž., Roskopf, C. M. & Parise, M. (2017). Variations in the susceptibility to landslides, as a consequence of land cover changes: a look to the past, and another towards the future. *Sci. Total Environ.* **601**, 1147–1159, <https://doi.org/10.1016/j.scitotenv.2017.05.231>.
- Potyondy, D. O. & Cundall, P. A. (2004). A bonded-particle model for rock. *Int. J. Rock Mech. Min. Sci.* **41**, No. 8, 1329–1364, <https://doi.org/10.1016/j.ijrmms.2004.09.011>.
- Pudasaini, S. P. & Mergili, M. (2019). A multi-phase mass flow model. *J. Geophys. Res. Earth. Surf.* **124**, No. 12, 2920–2942, <https://doi.org/10.1029/2019JF005204>.
- Reinaute, A., Malet, J. P., Maquaire, O., Ancey, C. & Locat, J. (2005). Flow behaviour and runout modelling of a complex debris flow in a clay-shale basin. *Earth Surf. Process Landf.: BGRG* **30**, No. 4, 479–488, <https://doi.org/10.1002/esp.1162>.

- Shan, T. & Zhao, J. (2014). A coupled CFD-DEM analysis of granular flow impacting on a water reservoir. *Acta Mech.* **225**, No. 8, 2449–2470, <https://doi.org/10.1007/s00707-014-1119-z>.
- Song, D., Choi, C. E., Ng, C. W. W. & Zhou, G. G. D. (2018). Geophysical flows impacting a flexible barrier: effects of solid-fluid interaction. *Landslides* **15**, No. 1, 99–110, <https://doi.org/10.1007/s10346-017-0856-1>.
- Song, D., Choi, C. E., Ng, C. W. W., Zhou, G. G., Kwan, J. S., Sze, H. Y. & Zheng, Y. (2019). Load-attenuation mechanisms of flexible barrier subjected to bouldery debris flow impact. *Landslides* **16**, No. 12, 2321–2334, <https://doi.org/10.1007/s10346-019-01243-2>.
- Song, D., Zhou, G. G., Chen, X. Q., Li, J., Wang, A., Peng, P. & Xue, K. X. (2021). General equations for landslide-debris impact and their application to debris-flow flexible barrier. *Engng Geol.* **288**, 106154, <https://doi.org/10.1016/j.enggeo.2021.106154>.
- Song, D., Bai, Y., Chen, X. Q., Zhou, G. G., Choi, C. E., Pasuto, A. & Peng, P. (2022). Assessment of debris flow multiple-surge load model based on the physical process of debris-barrier interaction. *Landslides* **19**, No. 5, 1165–1177, <https://doi.org/10.1007/s10346-021-01778-3>.
- Tan, D. Y., Yin, J. H., Feng, W. Q., Zhu, Z. H., Qin, J. Q. & Chen, W. B. (2019). New simple method for calculating impact force on flexible barrier considering partial muddy debris flow passing through. *J. Geotech. Geoenviron. Engng* **145**, No. 9, 04019051, [https://doi.org/10.1061/\(ASCE\)GT.1943-5606.0002133](https://doi.org/10.1061/(ASCE)GT.1943-5606.0002133).
- Tan, D. Y., Yin, J. H., Qin, J. Q., Zhu, Z. H. & Feng, W. Q. (2020). Experimental study on impact and deposition behaviours of multiple surges of channelized debris flow on a flexible barrier. *Landslides* **17**, No. 7, 1577–1589, <https://doi.org/10.1007/s10346-020-01378-7>.
- Tayyebi, S. M., Pastor, M., Yifru, A. L., Thakur, V. K. & Stickle, M. M. (2021). Two-phase SPH-FD depth-integrated model for debris flows: application to basal grid brakes. *Géotechnique*, <https://doi.org/10.1680/jgeot.21.00080>.
- Vagnon, F. & Segalini, A. (2016). Debris flow impact estimation on a rigid barrier. *Nat. Hazards Earth Syst. Sci.* **16**, No. 7, 1691–1697, <https://doi.org/10.5194/nhess-16-1691-2016>.
- Vicari, H., Ng, C. W. W., Nordal, S., Thakur, V., De Silva, W. R. K., Liu, H. & Choi, C. E. (2022). The effects of upstream flexible barrier on the debris flow entrainment and impact dynamics on a terminal barrier. *Can. Geotech. J.* **59**, No. 6, 1007–1019, <https://doi.org/10.1139/cgj-2021-0119>.
- Von Boetticher, A., Turowski, J. M., McArdell, B. W., Rickenmann, D. & Kirchner, J. W. (2016). Debrisintermixing-2.3: a finite volume solver for three-dimensional debris-flow simulations with two calibration parameters—part 1: model description. *Geosci. Model Dev.* **9**, No. 9, 2909–2923, <https://doi.org/10.5194/gmd-9-2909-2016>.
- Wendeler, C. (2016). *Debris-flow protection systems for mountain torrents*, WSL Berichte 44. Birmensdorf, Switzerland: Swiss Federal Institute for Forest, Snow and Landscape Research WSL.
- Wendeler, C., Volkwein, A., McArdell, B. W. & Bartelt, P. (2019). Load model for designing flexible steel barriers for debris flow mitigation. *Can. Geotech. J.* **56**, No. 6, 893–910, <https://doi.org/10.1139/cgj-2016-0157>.
- Xu, H., Gentilini, C., Yu, Z., Qi, X. & Zhao, S. (2018). An energy allocation based design approach for flexible rockfall protection barriers. *Engng Structs* **173**, 831–852, <https://doi.org/10.1016/j.engstruct.2018.07.018>.
- Yu, T. & Zhao, J. (2021). Semi-coupled resolved CFD-DEM simulation of powder-based selective laser melting for additive manufacturing. *Comput. Methods Appl. Mech. Engng* **377**, 113707, <https://doi.org/10.1016/j.cma.2021.113707>.
- Zhao, J. & Shan, T. (2013). Coupled CFD-DEM simulation of fluid-particle interaction in geomechanics. *Powder Technol.* **239**, 248–258, <https://doi.org/10.1016/j.powtec.2013.02.003>.
- Zhao, L., He, J. W., Yu, Z. X., Liu, Y. P., Zhou, Z. H. & Chan, S. L. (2020). Coupled numerical simulation of a flexible barrier impacted by debris flow with boulders in front. *Landslides* **17**, No. 12, 2723–2736, <https://doi.org/10.1007/s10346-020-01463-x>.
- Zhu, Z. H., Yin, J. H., Qin, J. Q. & Tan, D. Y. (2019). A new discrete element model for simulating a flexible ring net barrier under rockfall impact comparing with large-scale physical model test data. *Comput. Geotech.* **116**, 103208, <https://doi.org/10.1016/j.compgeo.2019.103208>.